

Stable, Surfactant-Free Graphene–Styrene Methacrylate Composite for Ultrafast Lasers

Felice Torrisi,* Daniel Popa, Silvia Milana, Zhe Jiang, Tawfique Hasan, Eleftherios Lidorikis, and Andrea C. Ferrari

Graphene–polymer composites play an increasing role in photonic and optoelectronic applications, from ultrafast pulse generation to solar cells. The fabrication of an optical quality surfactant-free graphene-styrene methyl methacrylate composite, stable to large humidity and temperature ranges is reported. The composite is tailored for photonic applications showing wavelength-independent linear absorption in the visible and near-infrared. When tested in a mode-locked laser, it allows the generation of stable ≈ 326 fs mode-locked pulses at 1550 nm, unperturbed by environmental conditions. The composite continues to operate as a saturable absorber even under complete water immersion at 60 °C. This confirms its stability against high-temperature and humidity.

1. Introduction

Rapid developments in photonics are fueled by advances in optical networks,^[1] broad-band systems,^[2] and ultrafast lasers.^[3] In particular laser sources producing nano- to subpicosecond pulses and are a key component in high-speed digital switching^[1] for optical communication technologies.^[4] Fiber lasers are attractive for their simple and compact designs,^[4] efficient heat dissipation,^[3] and alignment-free operation.^[3,5] These characteristics, combined with advances in glass technology^[6,7] and nonlinear optics,^[8] resulted in systems working from the visible to the mid-infrared (MIR) spectral region.^[6] In fiber lasers, ultrashort pulses can be obtained by passive mode-locking.^[4] This typically requires the aid of a nonlinear component called saturable absorber (SA).^[4,5,9] The key parameters of SAs are their dynamic response (the shorter the pulse, the faster the loss modulation^[9,10]) and its wavelength range (the broader the operation bandwidth, the shorter the supported pulses).^[9,10] In addition,

the global range of applications of ultrafast lasers (e.g., manufacturing, biomedical research, telecommunications, spectroscopy, etc.) requires SAs to show thermal and environmental stability (i.e., moisture absorption $\leq 1\%$ by weight in high, $\geq 80\%$, humidity environment and glass transition temperature ≥ 120 °C, for polymers).^[11] Carbon nanotubes (CNTs),^[2,12,13] graphene^[13–15] and recently, other 2D materials such as semiconducting transition metal dichalcogenides (MoS₂,^[16,17] WS₂,^[18] MoSe₂^[19]) and black phosphorus^[20,21] have emerged as promising SAs for ultrafast lasers.^[2,22–24] In CNTs, broadband operation is achieved by using a distribution of tube

diameters,^[2,22] while this is an intrinsic property of graphene.^[25] This, along with the ultrafast recovery time,^[26] low saturation fluence,^[15,27] and ease of fabrication^[28] and integration,^[29] makes graphene an excellent broadband SA.^[25] Consequently, mode-locked lasers using graphene SAs (GSAs) have been demonstrated from ≈ 800 nm^[30] to ≈ 970 nm,^[31] ≈ 1 μm ,^[32] ≈ 1.5 μm ,^[27] and ≈ 2 μm ^[33] up to ≈ 2.4 μm .^[34] Polymeric materials are the ideal solution to integrate GSAs into fiber lasers.^[1,35] They are easily processed by methods such as embossing, stamping, sawing, and wet or dry etching, and generally have a low-cost room-temperature fabrication process.^[13,36]

Liquid phase exfoliation (LPE) of graphite crystals in a surfactant-stabilized aqueous solution^[37–39] and organic solvents^[38,40,41] can be used to produce graphene. The LPE yield can be defined in different ways.^[29] The yield by weight, Y_M [%], is defined as the ratio between the weight of dispersed graphitic material and that of the starting graphite flakes. References [38,41,42] reported surfactant-free dispersions of graphene in organic solvents, e.g., *N*-methylpyrrolidone (NMP), *N*-dimethylformamide (DMF), and *ortho*-dichlorobenzene (*o*-DCB). Graphene from LPE is ideal to produce polymer composites as it can be mixed/blended in liquid or dry form with a host polymer matrix.^[13,38]

Polymers for composites used in fiber lasers for ultrashort pulse generation have to be transparent at the device-operation wavelength, be mechanically flexible, thermally, and chemically stable as well as being resistant to moisture (e.g., hydrophobic)^[13,35] as moisture-induced hygroscopic swelling in polymers can cause internal stress in the polymeric matrix.^[43] Various polymers, such as polyvinylacetate (PVAc),^[44] polyvinylalcohol (PVA),^[13] polymethylmethacrylate (PMMA),^[45] polyaniline (PANi),^[46] polycaprolactone (PCL),^[47] polyurethane (PU),^[48] polystyrene (PS),^[49] polylactide (PLA),^[50] polyethylene

Dr. F. Torrisi, Dr. D. Popa, Dr. S. Milana, Z. Jiang,
Dr. T. Hasan, Prof. A. C. Ferrari
Cambridge Graphene Centre
University of Cambridge
Cambridge CB3 0FA, UK
E-mail: ft242@cam.ac.uk



Prof. E. Lidorikis
Department of Materials Science and Engineering
University of Ioannina
Ioannina GR-45110, Greece

This is an open access article under the terms of the Creative Commons Attribution License, which permits use, distribution and reproduction in any medium, provided the original work is properly cited.

DOI: 10.1002/adom.201500760

terephthalate (PET),^[51] and polyvinylidene fluoride (PVDF),^[52] have been used as host matrix for graphene-based SAs. However, these polymer matrices have drawbacks, limiting their use. PVA, PVAc, PCL, and PET have a low glass-transition temperature, T_g (≈ 85 °C,^[53] ≈ 35 °C,^[54] ≈ 58 °C,^[55] and ≈ 80 °C,^[56] respectively), PMMA is brittle,^[57] and PANi and PCL are highly absorbing over the visible and infrared (IR) spectral range.^[58] PVA is unsuitable for humid environments (due to strong moisture absorption^[13,38,53]) and strongly absorbs in the 1300–1700 nm wavelength range (due to the presence of O–H bonds^[1,13]). Styrene methyl methacrylate (SMMA), a copolymer (i.e., based on monomers consisting of two polymer chains) of styrene ($C_6H_5CH=CH_2$) and methyl-methacrylate ($CH_2=C(CH_3)COOCH_3$)^[59] exhibits broadband optical transparency (from 200 to 3000 nm), high glass transition temperature ($T_g \geq 120$ °C,^[60]) and lower moisture absorption ($\leq 0.1\%$ by weight) with respect to PVA, PVAc, PET, and PCL,^[61] making it ideal for high humidity (up to 100%) and high temperature (up to 105 °C) environments.^[60,62–65] Moreover, the presence of styrene groups provides improved mechanical flexibility^[62] and thermal stability^[66,67] compared to widely used polymers such as PMMA, epoxy resins,^[35,68–72] and fluorinated polyimides.^[35,69–72]

The operating conditions that a SA based on a graphene-polymer composite can withstand primarily depend on the properties of the host polymer matrix. This should be transparent in the wavelength range of interest, so as to reduce nonsaturable losses^[12,13] and be environmentally stable, as temperature and moisture can adversely affect the SA performance.^[11] SMMA is thus a suitable candidate as a host matrix. Furthermore, the optimal SA composite must be free from cracks, bubbles, particles, aggregations, and other physical defects that affect the composite homogeneity, causing nonsaturable losses when the defect dimensions are comparable to the device-operation wavelength.^[73] The presence of defects depends on the SA manufacturing process. Defect-free polymer composites embedding graphene^[13,15,38] can be prepared from blends of soluble host polymers in a compatible graphene dispersion.^[13,38] SMMA is highly (>1.5 g mL⁻¹) soluble in NMP,^[61,74] which also exfoliates graphene effectively^[38,40,41] making it an ideal host polymer for defect-free, optical quality graphene-polymer composites. Here we utilize SMMA to fabricate stable and surfactant-free graphene-SMMA composites. We then use these as SAs for ultrashort (≈ 326 fs) optical pulse generation at 1550 nm achieved in a fiber laser cavity. The graphene-SMMA SA maintains stable (up to 1800 mins) pulse generation under water immersion and temperatures up to ≈ 60 °C demonstrating its temperature and humidity resistance.

2. Results and Discussion

2.1. Graphene Dispersion

Graphite flakes (NGS Naturgraphit) are exfoliated in an ultrasonic bath (Decon bath FS100, 100 W) for 9 h using anhydrous NMP as solvent. We use NMP for two reasons. First, SMMA is soluble in NMP.^[61] Second, graphene can be exfoliated in NMP,^[40] with no need of surfactants.^[38,40] The unexfoliated flakes are then allowed to settle for 10 min after sonication in

a sealed bottle. The graphene dispersion is then placed in an ultracentrifuge at 10 000 rpm (17 000 g) for an hour. We select this exfoliation sonication and centrifugation steps because they produce the highest Y_M in NMP.^[41] The top 70% is decanted for characterization and composite fabrication.

Optical absorption spectroscopy (OAS) is used to estimate the concentration of graphitic flakes^[37,39,40] by the Beer–Lambert Law: $A = \alpha cl$, where A is the absorbance, l [m] is the light path length, c [g L⁻¹] is the concentration of dispersed graphitic material and α [L g⁻¹ m⁻¹] is the absorption coefficient.^[38,40] Different values of α have been estimated both for aqueous^[37,75] (1390 L g⁻¹ m⁻¹ ref. [37]; 6600 L g⁻¹ m⁻¹ ref. [75]) and nonaqueous-based dispersions.^[40] Reference^[40] derived $\alpha \approx 2460$ L g⁻¹ m⁻¹ for a variety of solvents, (including NMP) while later ref. [42] reported $\alpha \approx 3620$ L g⁻¹ m⁻¹ for NMP. Reference [75] assigned this discrepancy to the c difference of the two dispersions. However, α is independent on c , thus more work is needed to determine its exact value. Reference [37] estimated $\alpha \approx 1390$ L g⁻¹ m⁻¹ with a standard deviation $\leq 0.01\%$. We then use $\alpha \approx 1390$ L g⁻¹ m⁻¹ in this work. **Figure 1a** plots the absorption spectrum of our LPE graphene dispersion diluted to 10% measured with a Perkin–Elmer Lambda 950 spectrometer with 1.3 nm resolution. Dilution is needed to avoid possible scattering losses at higher concentrations.^[37,75] The peak in the UV region is a signature of the van Hove singularity in the graphene density of states.^[76] Utilizing $\alpha \approx 1390$ L g⁻¹ m⁻¹, we estimate $c \approx 0.2$ g L⁻¹.

We then characterize the dispersion via high resolution transmission electron microscopy (HRTEM) using a Tecnai T20 high resolution electron microscope. **Figure 1b** shows a bright field micrograph of a partially folded Single Layer Graphene (SLG) flake on a TEM grid. The number of layers, N , can be counted from the zoomed-in high-resolution images of the edges.^[40,42] Statistics of N and flake size is performed by combined electron diffraction and bright field analyses.^[40,41] We find that $\approx 28\%$ are SLGs, $\approx 20\%$ are bilayer graphene (BLGs) flakes, and $\approx 52\%$ few layer graphene flakes (**Figure 1c**), with lateral size ≈ 300 – 1000 nm.

Raman spectroscopy is utilized to characterize and monitor step by step the fabrication of the graphene-SMMA composite, from the initial graphite to the final composite. Raman spectra are acquired at 457, 514, and 633 nm excitation wavelengths. The Raman spectrum of a starting natural graphite flake measured at 514 nm (shown in **Figure 2a**, blue curve) is compared to that of the LPE graphene dispensed on Si/SiO₂ and annealed at 170 °C to remove NMP (**Figure 2a**, green curve). In bulk graphite, the two most intense features are the G peak at ≈ 1580 cm⁻¹ and the 2D peak at ≈ 2700 cm⁻¹, while no D peak (at ≈ 1350 cm⁻¹) is observed. The G peak corresponds to the E_{2g} phonon at the Brillouin zone center.^[77] The D peak is due to the breathing modes of sp² rings and requires a defect for its activation by double resonance (DR).^[77–80] The 2D peak is the second order of the D peak.^[77] This is a single band in SLG, whereas it splits in four components in BLG, reflecting the evolution of the band structure.^[78] In bulk graphite it consists of two components, roughly 1/4 and 1/2 the height of the G peak, respectively.^[78] The 2D peak is always seen, even when no D peak is present, since no defects are required for the activation of two phonons with the same momentum, one backscattering

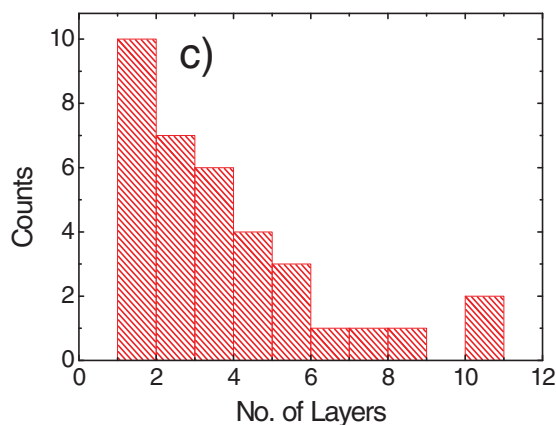
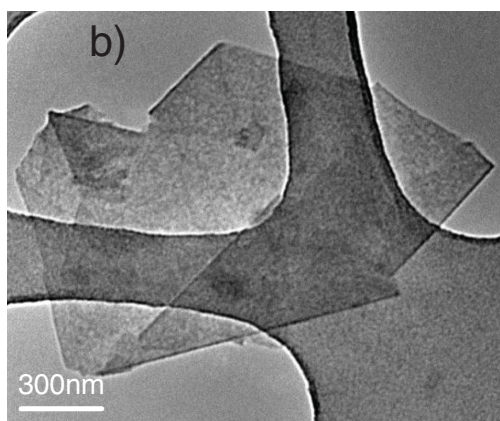
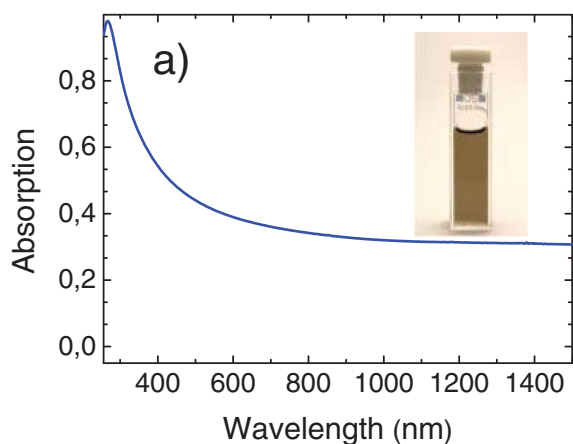


Figure 1. a) OAS spectrum of LPE graphene dispersion in NMP (inset shows a picture of graphene liquid dispersion). b) TEM bright field micrograph of dispersion-cast SLG. c) Statistics of number of layers of LPE graphene dispersion measured using TEM.

from the other. DR can also happen intravalley (i.e., connecting two points belonging to the same cone around K or K'), giving rise to the D' peak. In the Raman spectrum of LPE graphene significant D and D' bands are also present, besides the G and $2D$ peaks.^[79] We assign the D and D' peaks to the edges of the submicrometer flakes,^[81] rather than to the presence of a large amount of disorder within the flakes. The full width at half maximum of the G peak, $FWHM(G)$, always increases with disorder.^[82,83] In disordered carbons the G peak position, $Pos(G)$, increases with decreasing excitation wavelength,

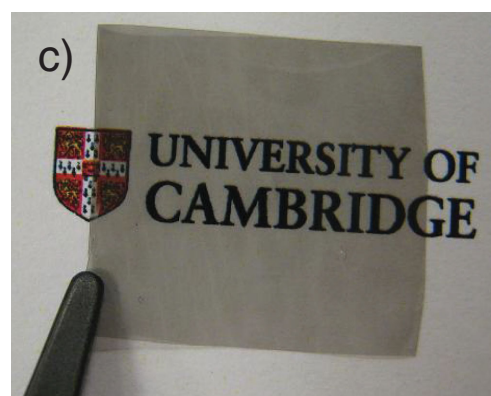
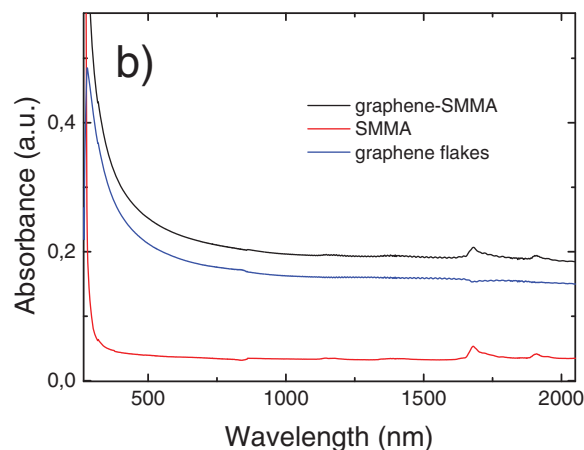
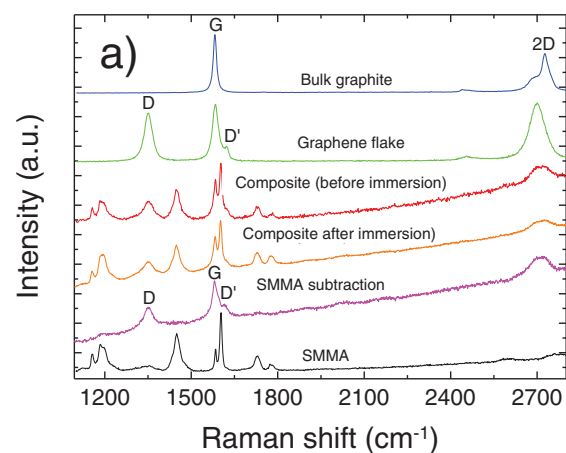


Figure 2. a) Raman spectra of starting natural graphite (blue), LPE graphene dispersion (green), graphene-SMMA composite before immersion (red), graphene-SMMA composite after immersion (orange), graphene-SMMA composite (magenta) after subtraction of the pure SMMA spectrum (black), revealing the characteristic D , G , D' , $2D$ peaks of LPE graphene. b) OAS spectra of the graphene-SMMA (black) composite, pure SMMA (red), and graphene flakes (blue). c) Optical image of the graphene-SMMA composite.

from IR to ultraviolet (UV).^[79] Thus, the G peak dispersion, $Disp(G) = \Delta Pos(G)/\Delta \lambda_L$, where λ_L is the laser excitation wavelength, increases with disorder. Combining the intensity ratio of the D and G peaks, $I(D)/I(G)$, with $FWHM(G)$ and $Disp(G)$, allows us to discriminate between disorder localized at the edges, and disorder in the bulk of the samples.^[41] In the latter

case, a higher $I(D)/I(G)$ would correspond to higher FWHM(G) and $\text{Disp}(G)$. $\text{Disp}(G) \approx 0.02 \text{ cm}^{-1} \text{ nm}^{-1}$ for our LPE graphene is much lower than in disordered carbons.^[84] Moreover, the distributions of $\text{Disp}(G)$, $I(D)/I(G)$ and FWHM(G) are not correlated, as also reported in ref. [41] where similar LPE graphene dispersions were analyzed.

Such absence of correlation is a clear indication that the major contribution to the D peak comes from the sample edges^[41] and further confirms the absence of defective flakes.

The 2D peak is a single Lorentzian, but larger than that of an individual graphene flake. Thus, even if the flakes are multilayers, they are electronically decoupled and, to a first approximation, behave as a collection of single layers.^[38,79,81]

2.2. Graphene–SMMA Composite

We prepare the graphene–SMMA SA as follows. SMMA (200 mg) is dissolved in NMP (8 mL) by mechanical stirring (this generates a homogeneous blend of SMMA in NMP). The SMMA solution is mixed with the LPE graphene dispersion. NMP is left to evaporate overnight in a vacuum chamber and the resulting composite is then baked in oven at 80 °C, producing a $\approx 55 \mu\text{m}$ freestanding graphene–SMMA polymer composite.

We also prepare a graphene–PVA SA following ref. [15] for stability performance comparison. Figure 2a plots the Raman spectrum of the graphene–SMMA composite (red curve) and that of pure SMMA (black curve), both measured at 514 nm.

While the D and 2D peaks are visible in the graphene–SMMA composite spectrum at $\approx 1350 \text{ cm}^{-1}$ and $\approx 2700 \text{ cm}^{-1}$, respectively, the G and D' bands are convoluted within two intense Raman features, located at $\approx 1585 \text{ cm}^{-1}$ and $\approx 1604 \text{ cm}^{-1}$, due to the stretching modes of carbon rings in SMMA.^[85,86] However, similarly to the LPE graphene flakes discussed above, it is still possible to estimate $\text{Pos}(G)$, and thus derive $\text{Disp}(G)$, as follows. The Raman spectrum of the graphene–SMMA composite and that of pure SMMA are acquired using identical exposure time and incident laser power; therefore, an accurate point-to-point subtraction of the SMMA reference spectrum from the graphene–SMMA composite spectrum can be implemented, Figure 2a (magenta curve). $\text{Disp}(G)$ is found to be $\approx 0.03 \text{ cm}^{-1} \text{ nm}^{-1}$.

This very small value (compared to $>0.1 \text{ cm}^{-1} \text{ nm}^{-1}$, expected for disordered carbons) indicates once again absence of in-plane defects within the graphene flakes embedded in the SMMA polymer matrix. Thus, SMMA does not affect the structure of the embedded flakes. OAS (Figure 2b, multiple colors) of SMMA, Graphene flakes and Graphene–SMMA composite reveal a featureless absorbance from 500 to 2000 nm for the three materials with a constant value of ≈ 0.2 for the composite (Figure 2c), compliant with the optical requirements of SA based on a graphene–polymer composite.^[12,13]

Optical microscopy is used to confirm the absence of cracks, bubbles, and aggregates within the composite, Figure 3a. This confirms the absence of defects having size comparable to or larger than the device-operation wavelength and the uniformity of the graphene–SMMA SA, once positioned on top of the fiber core (Figure 3a, inset). Figure 3b shows the SEM micrograph of a lateral cross-section of graphene–SMMA SA. The image

presents a visible layered structure of the composite with a preferential horizontal orientation.

Thermogravimetric Analysis (TGA) in N_2 gas is used to investigate the thermal stability of the graphene–SMMA composite. Figure 3c (red curve) shows the thermogram (weight loss as a function of temperature) of pure SMMA film, revealing a first $\approx 10\%$ weight loss peaked at $\approx 150 \text{ °C}$ which is attributed to water loss^[87] and a second weight drop of $\approx 90\%$ at $\approx 380 \text{ °C}$ which is consistent with the thermal decomposition of the polymer.^[63,87] The thermogram of LPE graphene (Figure 3c, blue curve) is almost featureless between 25 and 780 °C while followed by a gradual weight loss of about 5% (in the range 780–900 °C), typical of graphene flakes.^[88] The thermogram of

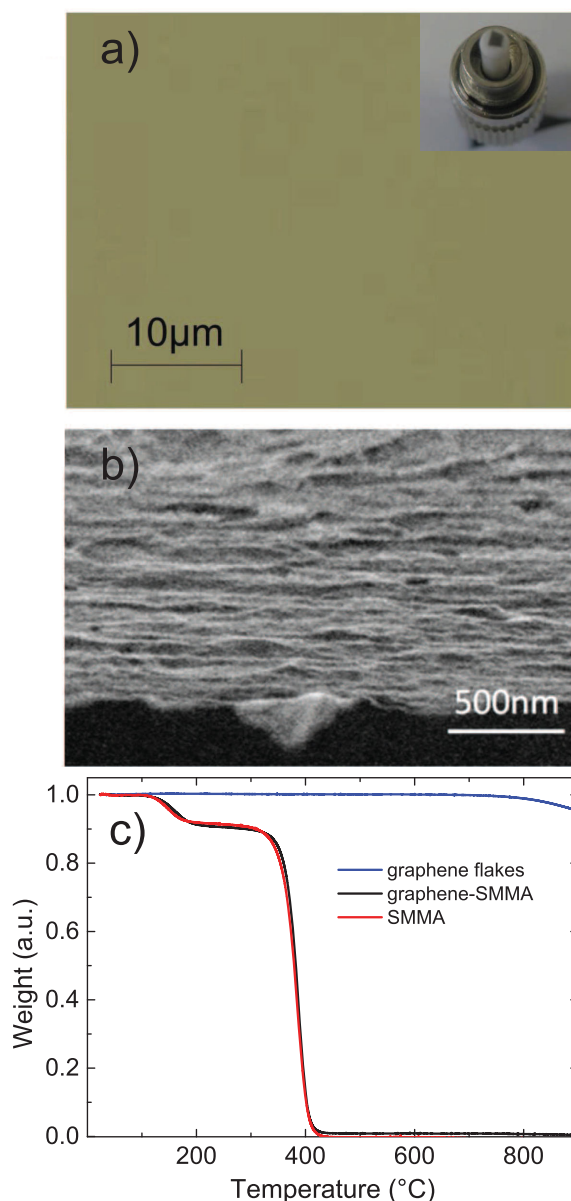


Figure 3. a) Optical micrograph and b) SEM micrograph cross-section of the graphene–SMMA SA. c) Thermogram of the pure SMMA (red curve), graphene flakes (blue curve), and the graphene–SMMA (black curve) composite.

graphene-SMMA composite contains both the TGA features of the pure SMMA and those of LPE graphene showing weight losses of $\approx 10\%$ and $\approx 89.9\%$ at $\approx 150\text{ }^\circ\text{C}$ and $\approx 380\text{ }^\circ\text{C}$, respectively. The residual weight of $\approx 0.1\%$ gradually decays in the range $780\text{--}900\text{ }^\circ\text{C}$ and can be attributed to graphene flakes in the composite. This confirms the thermal stability of our graphene-SMMA composite to up to $\approx 380\text{ }^\circ\text{C}$, higher than previous works reporting thermal degradation in N_2 at $\approx 120\text{ }^\circ\text{C}$ for a graphene-PVC composites^[60] and at $\approx 320\text{ }^\circ\text{C}$ for a graphene-PVA composites.^[53] The ratio of graphene mass (m_{gr}) in the composite over total graphene-SMMA composite mass ($m_{\text{gr-SMMA}}$) $m_{\text{gr}}/m_{\text{gr-SMMA}}$, can be approximated to $m_{\text{gr}}/m_{\text{SMMA}}$, where m_{SMMA} is the mass of SMMA (given that $m_{\text{gr}} \ll m_{\text{SMMA}}$).

Figure 3c shows that $m_{\text{gr}}/m_{\text{SMMA}} \approx 0.1\%$ at $\approx 500\text{ }^\circ\text{C}$, assuming the density of graphene $\rho_{\text{gr}} \approx 2.3\text{ g cm}^{-3}$ similar to that of graphite^[89] and the density of SMMA $\rho_{\text{SMMA}} \approx 1.09\text{ g cm}^{-3}$,^[90] we can estimate a graphene/SMMA volume fraction $\varphi_{\text{gr}}/\varphi_{\text{SMMA}} \approx 0.04\%$.

Reference [91] used the transfer matrix formalism^[92] to estimate N in a graphene-PVA SA. We apply this formalism to calculate, as a function of N , the reflection of our $55\text{ }\mu\text{m}$ free-standing graphene-SMMA composite film, where the SLGs (assumed horizontal for simplicity) are distributed in a random

fashion within a SMMA matrix. The SMMA refractive index is $n_{\text{SMMA}} \approx 1.53$, almost dispersion-less and lossless across the vis-IR wavelength range. In order to avoid coherent multiple reflections due to a specific arrangement of the flakes in the composite, we perform a statistical sampling by repeating each calculation for many (≈ 2000) random graphene distributions within the film. By comparing our calculations (Figure 4a, red curve), with the experimental absorption A (Figure 4a, black curve),^[91] we estimate that a 27% overall absorption translates to $N \approx 20$. A similar agreement around this value is evinced from Figure 4b, where the simulation is compared with a linear superposition approximation based on $A \approx N\pi\alpha/n_{\text{SMMA}}$, with α the fine structure constant. It is also worth noting that $N \approx 20$ corresponds to a total equivalent thickness (considering perfectly aligned monolayers) $t_{N=20} \approx 6.6\text{ nm}$. In this case, the $\varphi_{\text{gr}}/\varphi_{\text{SMMA}}$ can be estimated considering the graphene/SMMA thickness ratio ($t_{N=20}/t_{\text{SMMA}}$) per equivalent area (being $t_{N=20} \ll t_{\text{SMMA}}$), resulting in $\varphi_{\text{gr}}/\varphi_{\text{SMMA}} \approx 0.01\%$ which falls in the same order of magnitude of the volume fraction estimated by TGA. The difference between the two values of $\varphi_{\text{gr}}/\varphi_{\text{SMMA}}$ estimated by TGA and optical absorption is attributed to the limit of resolution of the two characterization instruments.

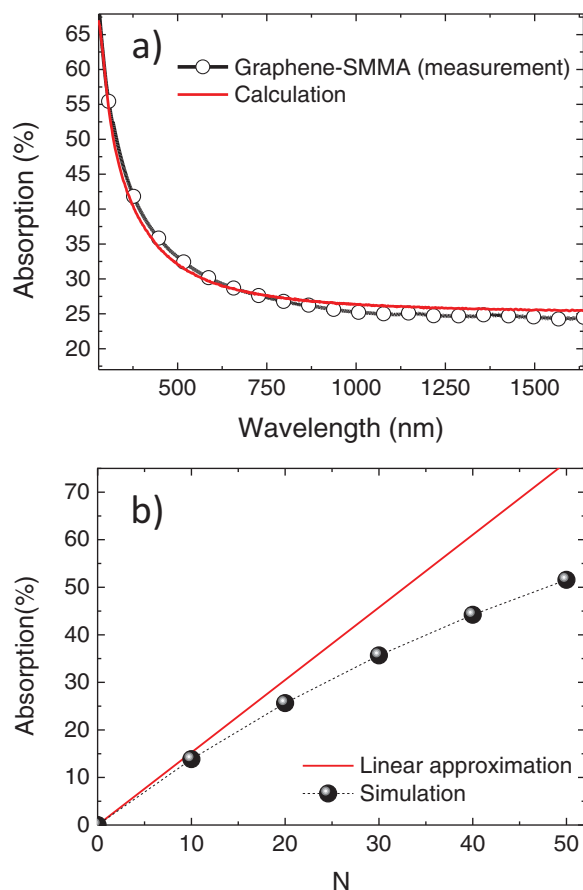


Figure 4. a) Experimental (black curve) and calculated (red curve) absorption of the graphene-SMMA SA for $N \approx 20$. b) Simulated (black dashed-dotted curve) absorption and estimated (red curve) absorption based on the $A \approx N\alpha/n_{\text{SMMA}}$ linear approximation.

2.3. Graphene-SMMA Mode-Locked Fiber Laser

The graphene-SMMA composite is used to mode-lock a fiber laser. For our experiment, we use a fiber laser with anomalous negative dispersion.^[15] We first measure its nonlinear optical transmittance as a function of the input pump power, Figure 5a, using a 600 fs pulse source with 4 MHz repetition rate at 1550 nm. The maximum optical fluence is $140\text{ }\mu\text{J cm}^{-2}$, corresponding to a $\approx 0.9\%$ change in transmittance, typical of graphene-polymer SAs^[15] and comparable to that observed in other 2D material-polymer SAs (such as MoS_2).^[93] The graphene-SMMA SA is then inserted into a fiber laser device to form the mode-locker (Figure 5b). The laser setup (Figure 5b) is a ring cavity pumped by a 980 nm laser diode (LD) via a wavelength division multiplexer (WDM), with 1.25 m erbium doped fiber (EDF) as the gain medium. Unidirectional operation of the cavity is ensured by an optical isolator (ISO). A polarization controller (PC) is inserted into the cavity for the optimization of the intracavity polarization state. The laser output is directed through a 20% port of an output coupler. Figure 6a plots the optical spectrum. The full width at half maximum (FWHM) of the output spectrum is 9.8 nm. The spectrum features side-bands, which are typical characteristics of soliton-like pulse formation due to periodical intracavity perturbations.^[94] The autocorrelation trace of the output pulses (Figure 6b), measured by a second harmonic generation (SHG) autocorrelator, shows a FWHM of $\approx 502\text{ fs}$; using a sech^2 temporal fitting, a $\approx 326\text{ fs}$ pulse width is obtained after deconvolution. The time bandwidth product (TBP), the product of pulse duration (in seconds) and spectral width (in Hertz) is a measure of the output pulse quality.^[15,95] We obtained $\text{TBP} \approx 0.33$, close to the theoretical value of 0.315 for transform-limited sech^2 pulses.^[95] The spectral width, pulse duration, and TBP are comparable to those of previous graphene mode-locked fiber lasers.^[15,27,36]

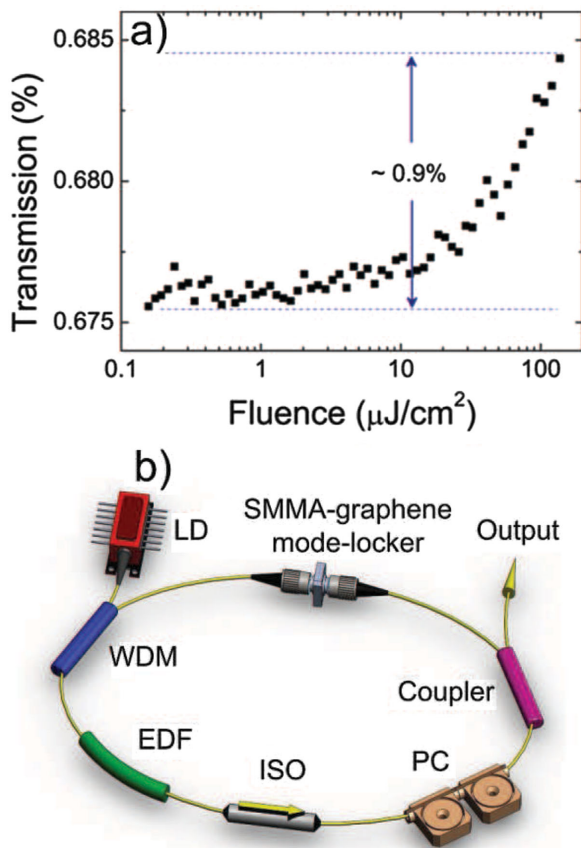


Figure 5. a) Transmission of the graphene-SMMA composite as a function of the input optical fluence. b) Scheme of the fiber laser setup. Laser diode (LD), wavelength division multiplexer (WDM), erbium-doped fiber (EDF), isolator (ISO), and polarization controller (PC).

2.4. Stability of Graphene–Polymer Mode-Locker

We then investigate the laser operation stability against different environmental conditions. We use both graphene-SMMA and graphene-PVA SAs (prepared as in ref. [15]) to mode-lock the same fiber laser setup (Figure 5b) at $\approx 21^\circ\text{C}$ and $\approx 40\%$ humidity. Both show stable mode-locking over more than 30 h. We then repeat the measurement with the graphene-PVA mode-locker completely immersed in water at $\approx 60^\circ\text{C}$ to simulate accelerated adverse environmental conditions (Figure 7). Under these extreme conditions, after ≈ 38 min the laser switches to continuous wave (CW) operation (Figure 8a). The corresponding spectra of the laser operation in this case after 10, 32, and 40 min (shown in Figure 8b) show three distinct behaviors: mode-locking (black curve); CW breakthrough (red curve); and CW (blue curve). We attribute this to the solubility of PVA in water.^[61] On the other hand, the graphene-SMMA modelocked laser shows stable continuous mode-locking (Figure 8c) for more than 1800 min under water immersion. Optical output spectra of the SMMA-graphene laser acquired after 600 min (black curve), 1200 min (red curve), and 1800 min (blue curve) (Figure 8d) show no significant difference. This indicates no effect on the composite stability with the changes in temperature (≈ 21 – 60°C) and humidity (≈ 40 – 100%).

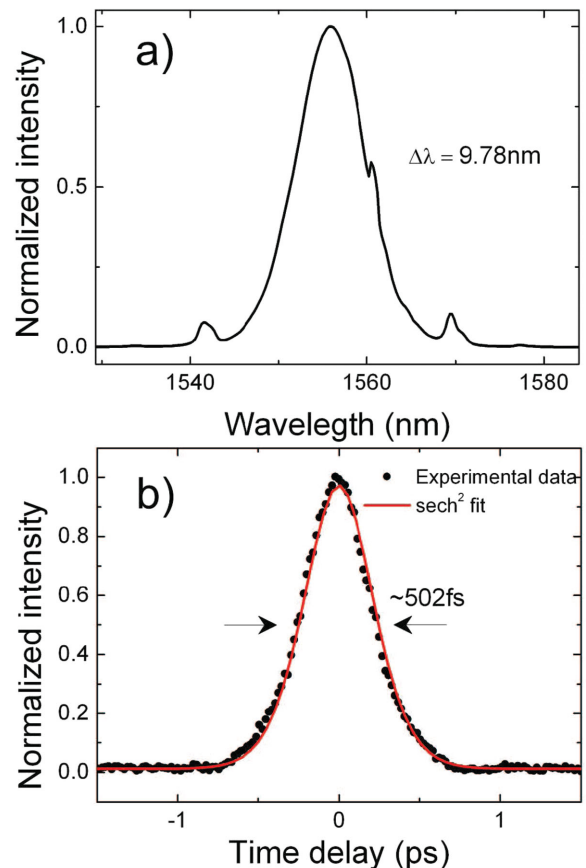


Figure 6. Output characteristics of ultrafast lasers mode-locked by graphene-SMMA SA. a) Optical spectrum with bandwidth 9.8 nm. b) Auto-correlation trace with sech^2 fit.

The above observation is corroborated by Raman analysis. We characterize the graphene-PVA SA by Raman spectroscopy, before and after the laser operation under water immersion (≈ 60 min laser running). Figure 9a,b plots the Raman spectra (black curve) of the optical fiber (Corning SMF-28 Ultra Optical

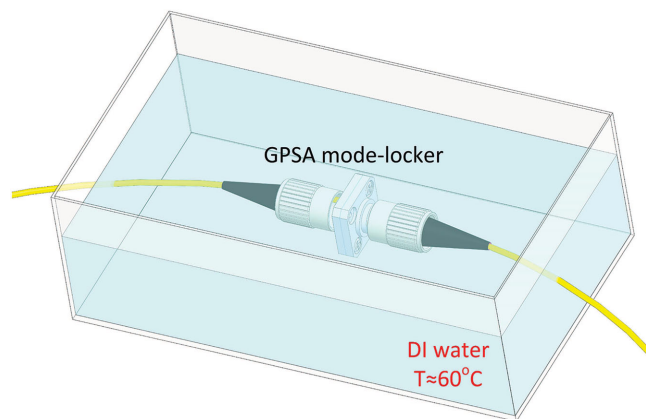


Figure 7. Scheme of GPSA mode-locker immersed in water at $T \approx 60^\circ\text{C}$ to simulate accelerated adverse environmental conditions.

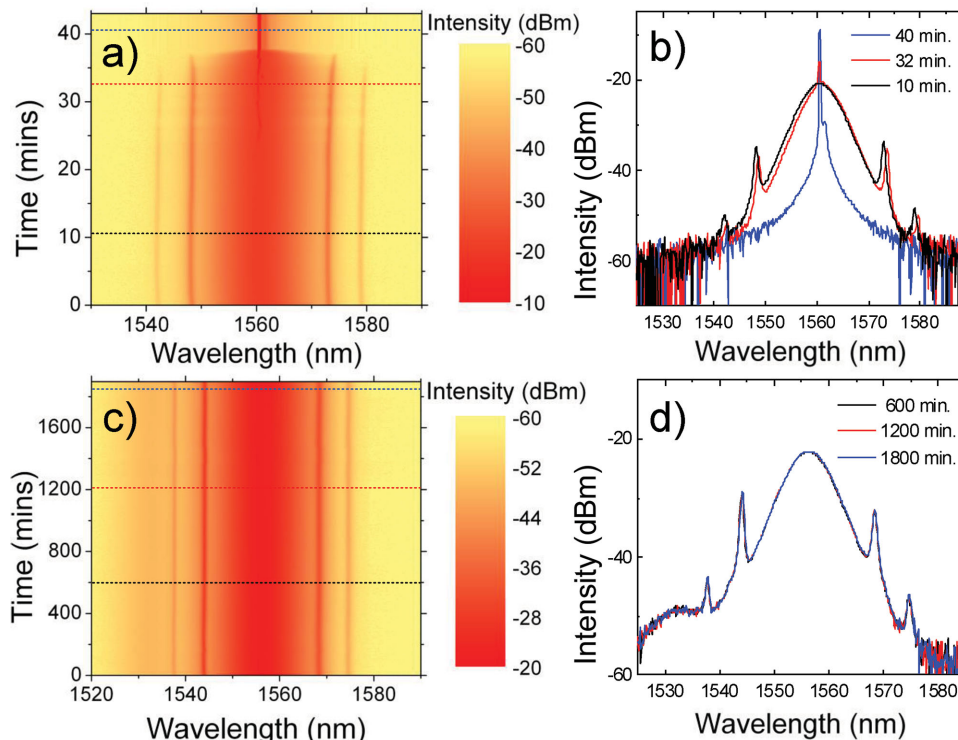


Figure 8. a) Spectra as function of time for PVA-graphene laser under water immersion. b) Optical spectra of PVA-graphene laser acquired after 10 min (black curve), 32 min (red curve), and 40 min (blue curve) of water immersion, respectively. c) Spectra as function of time for SMMA-graphene laser under water immersion. d) Optical spectra of SMMA-graphene laser acquired after 600 min (black curve), 1200 min (red curve), and 1800 min (blue curve) of water immersion, respectively.

Fiber), featuring the Si–O stretching ($\approx 1000\text{ cm}^{-1}$) and bending ($\approx 500\text{ cm}^{-1}$) modes typical of glassy silicates.^[96] The red curve of Figure 9a (also zoomed in Figure 9b, for clarity) corresponds to the Raman spectrum of pure PVA (red curve). This is characterized by an intense band at $\approx 2800\text{--}3200\text{ cm}^{-1}$, corresponding to the C–H symmetric and antisymmetric stretching vibrations of CH_2 and CH_3 functional groups in PVA.^[86,97–99] The

peak at $\approx 1730\text{ cm}^{-1}$ is attributed to C=O stretching modes,^[97–99] whereas the weaker bands at $\approx 1443\text{ cm}^{-1}$ and 1357 cm^{-1} are due to CH_2 antisymmetric and symmetric deformation, respectively.^[97–99] The peak at $\approx 1139\text{ cm}^{-1}$ is due to C–O stretching,^[97–99] and the weak bands in the spectral region $\approx 850\text{--}920\text{ cm}^{-1}$ arise from C–C stretching modes.^[97–99] The peak at $\approx 632\text{ cm}^{-1}$ corresponds to C=O out-of-plane bending

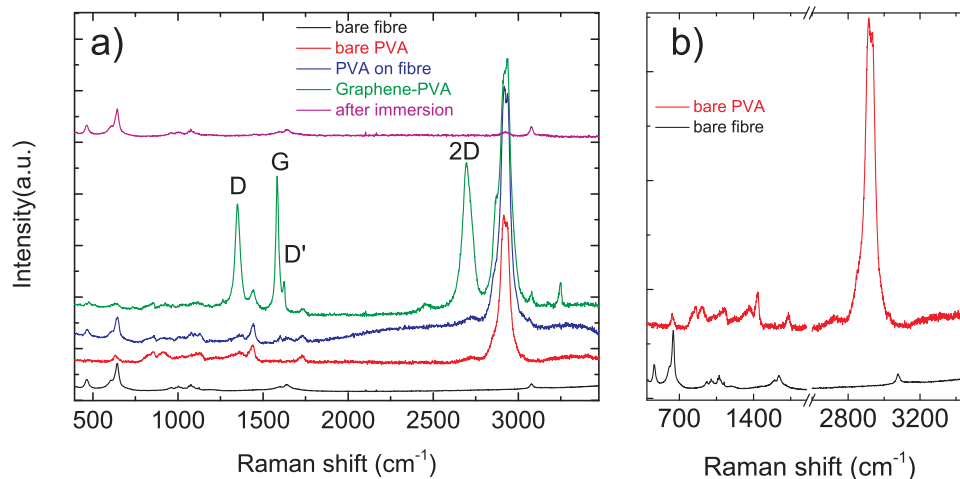


Figure 9. a) Raman spectra of optical fiber (black curve), PVA polymer (red curve), PVA polymer placed on the optical fiber (blue curve), graphene-PVA composite (green curve) on the optical fiber, before immersion in water, and graphene-PVA composite (magenta curve) on the optical fiber, after immersion in water. b) A zoom-in of the Raman spectra of the optical fiber (black curve) and PVA polymer (red curve) shown in a).

modes.^[97–99] The Raman spectrum of PVA placed on the optical fiber (blue curve, Figure 9a) contains both the Raman features of the fiber and those of pure PVA. The spectrum of the graphene-PVA composite (green curve) placed on the optical fiber confirms the presence of graphene flakes, as indicated by the D, G, D', and 2D peaks. The overall spectrum is in fact a superposition of that of the graphene flakes (Figure 2a, green curve), that of the pure PVA, and that of the optical fiber. The magenta curve in Figure 9 corresponds to the Raman spectrum measured on the same position on the optical fiber after mode-locking failure in water immersion (≈ 60 min). The Raman signatures of the optical fiber are evident by comparing this Raman spectrum with that of the optical fiber (black curve). After a point-to-point subtraction of the Raman spectrum of the fiber (black curve) from the Raman spectrum of the composite after immersion (magenta curve), no D, D', G, and 2D peaks could be detected. A weak additional mode at ≈ 2900 cm^{-1} is present, attributed to residual PVA on the fiber. This indicates that water can indeed penetrate through the fiber connectors and reach the composite sandwiched in between. On the other hand, when a graphene-SMMA SA is used as mode-locker immersed in water at ≈ 60 °C, the laser operation is stable for a long time (more than 1800 min) under water immersion, Figure 8c. Figure 8d shows stable optical spectra of graphene-SMMA SA after 600 min (black curve), 1200 min (red curve), and 1800 min (blue curve) of water immersion, respectively. Raman analysis of the graphene-SMMA SA before (Figure 2a, red curve) and after (Figure 2a, orange curve) the laser operation under water immersion (more than 1800 min) confirms no change of the graphene-SMMA SA. Our results show that the graphene-SMMA SA can withstand high humidity and temperature conditions, offering a stable mode-locking over long time. On the other hand graphene-PVA SA (well known polymer SA for photonics) is damaged by water and high temperature, resulting in abrupt mode-locking cessation.

3. Conclusion

We fabricated a homogeneous surfactant-free graphene-SMMA composite and shown its viability as SA. SMMA provides high optical transparency of the host polymer in the visible-IR range and superior thermal stability. We also reported a Erbium-doped Fiber Laser mode-locked by graphene-SMMA composite, at room conditions and under water immersion at 60 °C for more than 1800 min. Such a high stability of the graphene-SMMA composite under adverse environmental conditions along with its excellent nonlinear properties could provide a simple, low-cost optical component for ultrastable photonic devices.

Acknowledgements

The authors acknowledge funding from the ERC synergy grant Hetero2D, the EU Graphene Flagship (Grant No. 604391), a Royal Society Wolfson Research Merit Award, the EPSRC grants EP/K01711X/1, EP/K017144/1, EP/L016087/1, and the EU FP7 project MEM4WIN. T.H.

acknowledges support from a RAEng Research Fellowship (Graphlex). D.P. acknowledges support from Emmanuel College, Cambridge.

Received: December 17, 2015

Revised: February 18, 2016

Published online: April 1, 2016

- [1] H. Ma, A. K. Y. Jen, L. R. Dalton, *Adv. Mater.* **2002**, *14*, 1339.
- [2] F. Wang, A. G. Rozhin, V. Scardaci, Z. Sun, F. Hennrich, I. H. White, W. I. Milne, A. C. Ferrari, *Nat. Nanotechnol.* **2008**, *3*, 738.
- [3] F. Dausinger, F. Lichtner, H. Lubatschowski, *Top. Appl. Phys.* **2003**, *96*, 326.
- [4] M. E. Fermann, I. Hartl, *Nat. Photonics* **2013**, *7*, 868.
- [5] M. E. Fermann, A. Galvanauskas, G. Sucha, *Ultrafast lasers: Technology and Applications*, Marcel Dekker, New York, USA **2003**.
- [6] M. J. F. Digonnet, *Rare Earth Doped Fiber Lasers and Amplifiers*, Marcel Dekker, New York, USA **1993**.
- [7] P. Russell, *Science* **2003**, *299*, 358.
- [8] J. M. Dudley, J. R. Taylor, *Nat. Photonics* **2009**, *3*, 85.
- [9] U. Keller, *Nature* **2003**, *424*, 831.
- [10] O. Okhotnikov, A. Grudinin, M. Pessa, *New J. Phys.* **2004**, *6*, 177.
- [11] A. Chong, W. H. Renninger, F. W. Wise, *Opt. Lett.* **2008**, *33*, 1071.
- [12] V. Scardaci, Z. P. Sun, F. Wang, A. G. Rozhin, T. Hasan, F. Hennrich, I. H. White, W. I. Milne, A. C. Ferrari, *Adv. Mater.* **2008**, *20*, 4040.
- [13] T. Hasan, Z. Sun, F. Wang, F. Bonaccorso, P. H. Tan, A. G. Rozhin, A. C. Ferrari, *Adv. Mater.* **2009**, *21*, 3874.
- [14] Q. Z. Bao, H. Wang, Y. Ni, Z. Yan, Y. Shen, K. P. Loh, D. Y. Tang, *Adv. Funct. Mater.* **2009**, *19*, 3077.
- [15] Z. Sun, T. Hasan, F. Torrisi, D. Popa, G. Privitera, F. Wang, F. Bonaccorso, D. M. Basko, A. C. Ferrari, *ACS Nano* **2010**, *4*, 803.
- [16] M. Zhang, R. C. T. Howe, R. I. Woodward, E. J. R. Kelleher, F. Torrisi, G. Hu, S. V. Popov, J. R. Taylor, T. Hasan, *Nano Res.* **2015**, *8*, 1522.
- [17] R. I. Woodward, E. J. R. Kelleher, R. C. T. Howe, G. Hu, F. Torrisi, T. Hasan, S. V. Popov, J. R. Taylor, *Opt. Express* **2014**, *22*, 31113.
- [18] D. Mao, Y. Wang, C. Ma, L. Han, B. Jiang, X. Gan, S. Hua, W. Zhang, T. Mei, J. Zhao, *Sci. Rep.* **2015**, *5*, 7965.
- [19] R. I. Woodward, R. C. T. Howe, T. H. Runcorn, G. Hu, F. Torrisi, E. J. R. Kelleher, T. Hasan, *Opt. Exp.* **2015**, *23*, 20051.
- [20] D. Li, H. Jussila, L. Karvonen, G. Ye, H. Lipsanen, X. Chen, Z. Sun, *Sci. Rep.* **2015**, *5*, 15899.
- [21] H. Mu, S. Lin, Z. Wang, S. Xiao, P. Li, Y. Chen, H. Zhang, H. Bao, S. P. Lau, C. Pan, D. Fan, Q. Bao, *Adv. Opt. Mater.* **2015**, *3*, 1447.
- [22] R. Going, D. Popa, F. Torrisi, Z. Sun, T. Hasan, F. Wang, A. C. Ferrari, *Physica E* **2012**, *44*, 1078.
- [23] D. Popa, Z. Sun, T. Hasan, W. Cho, F. Wang, F. Torrisi, A. Ferrari, *Appl. Phys. Lett.* **2012**, *101*, 153107.
- [24] Z. Sun, D. Popa, T. Hasan, F. Torrisi, F. Wang, E. J. R. Kelleher, J. C. Travers, V. Nicolosi, A. C. Ferrari, *Nano Res.* **2010**, *3*, 653.
- [25] F. Bonaccorso, Z. Sun, T. Hasan, A. C. Ferrari, *Nat. Photonics* **2010**, *4*, 611.
- [26] D. Brida, A. Tomadin, C. Manzoni, Y. J. Kim, A. Lombardo, S. Milana, R. R. Nair, K. S. Novoselov, A. C. Ferrari, G. Cerullo, M. Polini, *Nat. Commun.* **2012**, *4*, 1987.
- [27] D. Popa, Z. Sun, F. Torrisi, T. Hasan, F. Wang, A. C. Ferrari, *Appl. Phys. Lett.* **2010**, *97*, 203106.
- [28] A. C. Ferrari, F. Bonaccorso, V. Falco, K. S. Novoselov, S. Roche, P. Boggild, S. Borini, F. Koppens, V. Palermo, N. Pugno, J. A. Garrido, R. Sordan, A. Bianco, L. Ballerini, M. Prato, E. Lidorikis, J. Kivioja, C. Marinelli, T. Ryhanen, A. Morpurgo, J. N. Coleman, V. Nicolosi, L. Colombo, A. Fert,

- [91] D. G. Purdie, D. Popa, V. J. Wittwer, Z. Jiang, G. Bonacchini, F. Torrisi, S. Milana, E. Lidorikis, A. C. Ferrari, *Appl. Phys. Lett.* **2015**, *106*, 253101.
- [92] M. Born, E. Wolf, *Principles of Optics: Electromagnetic Theory of Propagation, Interference and Diffraction of Light*, 7th expanded ed., Cambridge University Press, New York, USA **1999**.
- [93] R. I. Woodward, R. C. T. Howe, G. Hu, F. Torrisi, M. Zhang, T. Hasan, E. J. R. Kelleher, *Photon. Res.* **2015**, *3*, A30.
- [94] M. L. Dennis, I. N. Duling, *IEEE J. Quantum Electron* **1994**, *30*, 1469.
- [95] O. Svelto, *Principles of Lasers*, 4th ed., Plenum, New York, USA **1998**.
- [96] P. Colomban, A. Tournie, L. Bellot-Gurlet, *J. Raman Spectrosc.* **2006**, *37*, 841.
- [97] E. B. Wilson, J. C. Decius, P. C. Cross, *Molecular Vibrations*, Mc Graw Hill, New York, USA **1955**.
- [98] J. B. Lambert, H. F. Shurvell, R. G. Cooks, *Introduction to Organic Spectroscopy*, Macmillan, New York, USA **1987**.
- [99] K. B. Renuka Devi, R. Madivanane, *IRACST-Eng. Sci. Technol.* **2012**, *2*, 2250.
-